



Optical Monitoring and Spectral Analysis of OJ 287

Yu-Hai Yuan^{1,2} , Qi-Min Chen^{1,2}, Yi-Tao Liu^{1,2}, Bao-Yi Liang^{1,2}, Wen-Xin Yang^{1,2}, Le-Jian Ou^{1,2}, and Guo-Hai Chen^{1,2}

¹ Center for Astrophysics, Guangzhou University, Guangzhou, Guangdong 510006, People's Republic of China; yh_yuan@gzhu.edu.cn
² Astronomy Science and Technology Research Laboratory of Department of Education of Guangdong Province, Guangzhou 510006, People's Republic of China

Received 2025 February 11; revised 2025 October 14; accepted 2025 October 16; published 2025 November 25

Abstract

We present a comprehensive multiband optical monitoring and spectral analysis of the blazar OJ 287, conducted using the 1.26 m National Astronomical Observatory–Guangzhou University Infrared/Optical telescope (NGT). During an intensive 17 day observational campaign from 2022 December to 2023 January, we obtained 2716 high-quality photometric observations (929 in the *g* band, 887 in the *r* band, and 900 in the *i* band). The data reveal significant variability across all bands. Our main findings are as follows. (1) Significant magnitude variations were detected: $\Delta m_g = 0.945 \pm 0.048$ mag (*g* band), $\Delta m_r = 0.648 \pm 0.023$ mag (*r* band), and $\Delta m_i = 0.945 \pm 0.051$ mag (*i* band). (2) Numerous intraday variability (IDV) events were identified, with characteristic parameters (Δm , ΔT , and $VR = \frac{\Delta m}{\Delta T}$) showing consistent patterns between the *g* and *r* bands but distinct behavior in the *i* band. (3) Successful modeling of intraday light curves using a multi-Gaussian function, yielding brightening ($\Delta T'_b$) and dimming ($\Delta T'_d$) timescales, and revealing an average peak separation of $\Delta T_c = 42.96 \pm 0.99$ minutes that appears to be frequency independent. (4) Development of a novel radiation framework suggesting that the observed IDV phenomena originate from multiple components—with the frequency-independent variations attributable to the central black hole, while frequency-dependent variations stem from jet and accretion disk processes.

Unified Astronomy Thesaurus concepts: Blazars (164); CCD photometry (208); Active galaxies (17)

Materials only available in the online version of record: machine-readable table

1. Introduction

Blazars are a widely studied subclass of active galactic nucleus, characterized by a range of extreme observational properties, including core dominance, a nonthermal spectrum, superluminal motion, high and variable polarization, violent optical variability, and so on (M. H. Ulrich et al. 1997). Based on the compact radio morphologies and the optical spectrum (e.g., C. M. Urry & P. Padovani 1995; Z. R. Weaver et al. 2020), blazars can be separated into two categories: flat-spectrum radio quasars (FSRQs) and BL Lac objects; the former containing broad emission lines and the latter characterized by the featureless optical or weak emission line (M. Stickel et al. 1991). The above classification can be understood by the framework of matter flowing or passing through the accretion disk onto supermassive black holes (SMBHs; E. Wehrle Ann et al. 2019).

Among the extreme properties of blazars, optical variabilities can be directly observed, and can be classified into three subclasses: intraday variability (IDV, with timescales of less than 1 day), short-term variability (with timescales from days to months), and long-term variability (with timescales of years; J. H. Fan 2005). The IDV can originate from the central black hole, the interstellar medium, and the jet and accretion disk, and most IDVs display nonperiodic and irregular characteristics.

The relations between the brightness and spectral indices have been analyzed by many works (e.g., L. M. J. Brown et al. 1989; E. Massaro et al. 1998; M. F. Gu et al. 2006; J. H. Fan et al. 2014;

N. Kalita et al. 2023; Y. H. Yuan et al. 2023). Generally, BL Lac objects display a bluer-when-brighter (BWB) behavior, and most FSRQs display a redder-when-brighter (RWB) behavior (M. F. Gu et al. 2006). N. Kalita et al. (2023) and Y. H. Yuan et al. (2023) reported that these relations of BL Lacertae display the time evolution of color. Y. H. Yuan et al. (2023) found some uneven locations in the distributions between brightness and spectral indices of BL Lacertae, which should come from the ministructures of the jet, the shock-induced particle acceleration, or the magnetic reconnection in the jet.

Based on the locations of the synchrotron peak frequency, BL Lac objects can be classified as low-synchrotron-peaked BL Lac objects (LBLs, $\nu_{\text{syn}} < 10^{14}$ Hz), intermediate-synchrotron-peaked BL Lac objects ($\nu_{\text{syn}} \sim 10^{14}\text{--}10^{15}$ Hz), and high-synchrotron-peaked BL Lac objects (HBLs, $\nu_{\text{syn}} > 10^{15}$ Hz; A. A. Abdo et al. 2010). HBLs can be well described by a one-zone SSC model, and the other two classes are usually described by an external Compton model (A. Acharyya et al. 2024).

OJ 287 is a frequently studied blazar, located at a redshift of $z = 0.306$ (K. Nilsson et al. 2010). The synchrotron peak occurs in the near-infrared (J. H. Fan et al. 2016), so this source can be classed as an LBL. Throughout history, this source has been frequently observed, and the optical monitoring can be traced back to 1890 (A. Sillanpää et al. 1988). In some monitored programs, OJ 287 is a very important target. OJ-94 is an international research project, in which OJ 287 was one of the major targets from 1993 to 1997. This source is also one of the most important targets of the 1.26 m National Astronomical Observatory-Guangzhou University Infrared/Optical telescope (NGT).

Based on multiband observations, there have been many research works focusing on the optical variabilities of this source. E. Valtaoja et al. (1985) made use of radio



Original content from this work may be used under the terms of the [Creative Commons Attribution 4.0 licence](#). Any further distribution of this work must maintain attribution to the author(s) and the title of the work, journal citation and DOI.

observations to report a period of 15.7 minutes. Using the 7 mm light curve, W. M. Kinzel et al. (1988) reported a period of 35 minutes. In the optical band, A. Sillanpää (1991) reported a period of 9.3 days, J. H. Wu et al. (2006) reported a period of 40 days, G. Bhatta et al. (2016) reported a period of 400 days, and Y. H. Yuan et al. (2021) reported a period of 94 minutes. Using the observations from 2015 to 2023, A. C. Gupta et al. (2024) reported a large-amplitude flux variability of about 3.0 mag, and the large variability in the degree of polarization of about 37%.

Quasiperiodic behavior has been reported in many blazars, among which OJ 287 displayed the most convincing period of 12 yr (e.g., A. Sillanpää et al. 1988; L. Dey et al. 2018), or another possible period of \sim 22 yr (S. Britzen et al. 2018). Some models can explain these periods. For example, there is a precessing SMBH system at the center of this source (e.g., A. Sillanpää et al. 1988; M. J. Valtonen et al. 2011; R. Hudec et al. 2013), or that this source has a helical jet (S. Britzen et al. 2018). Based on the binary SMBH model, two black holes lie at the center; the masses of the primary and secondary black holes are $1.83 \times 10^{10} M_{\odot}$ and $1.5 \times 10^8 M_{\odot}$, respectively (L. Dey et al. 2018). However, A. Goyal et al. (2018) did not find the 12 yr periodicity based on the Fermi Large Area Telescope light curves.

Some works study the relations between the brightness and spectral indices of OJ 287. This source displays a BWB trend (e.g., Q. Guo et al. 2017; A. C. Gupta et al. 2019; Y. H. Yuan et al. 2021). But Y. G. Zheng et al. (2007) obtained a opposite trend: when the source became brighter, the spectra became redder over the 6 yr of observations. E. Bonning et al. (2012) found both the RWB and the BWB behaviors.

This paper is arranged as follows: in Section 2, we give the observations and data reductions; in Section 3, we perform the analyses of optical variabilities; in Section 4, we present the discussions and conclusions.

2. Observations and Data Reductions

The 1.26 m NGT is located at Xinglong station, National Astronomical Observatories, Chinese Academy of Sciences. This telescope is equipped with three SBIG STT-8300M cameras, a CCD of 3326×2504 pixels, and the view field of $6.^{\circ}0 \times 4.^{\circ}5$. The filters are standard Sloan Digital Sky Survey g , r , and i bands. J. H. Fan et al. (2019) gave a detailed description of this telescope.

The observed images contain bias, flat, dark, and target images. Data reduction was performed using the Automated Photometry Pipeline (W. R. Huang et al. 2020). The standard stars involved in this work are collected from M. Fiorucci & G. Tosti (1996), see Table 1.

The observations are calculated by the averaged values of differential photometries based on the whole comparison stars. Within the same frame, considering to every comparison star c_i , $i = 1-N$, we obtain the magnitude m_i for the object of interest.

At the given time, the object's magnitude should be

$$\bar{m} = \frac{\sum m_i}{N}, \quad (1)$$

here, N is the total number of comparison stars.

The standard deviation can be calculated by the following procedure. First, for any two comparison stars (c_i and c_j), their magnitudes were m_i and m_j and the magnitude difference

Table 1
Comparison Stars of OJ 287

Star	V (Error) (mag)	R (Error) (mag)	I (Error) (mag)
(1)	(2)	(3)	(4)
4	14.18(0.04)	13.74 (0.04)	13.28 (0.04)
10	14.60(0.05)	14.34 (0.05)	14.03 (0.05)
11	14.94(0.04)	14.65 (0.05)	14.32 (0.05)

Note. Column (1): the label of comparison stars. Column (2): the magnitudes with errors at the V band. Column (3): the magnitudes with errors at the R band. Column (4): the magnitudes with errors at the I band.

between them was $\Delta m_{ij} = m_i - m_j$, with the standard deviation being σ_{ij} . Second, we compared the standard deviation σ from two arbitrary standard stars, and found that when the comparison stars were “10” and “11,” the standard deviation reached the minimum. Third, we chose the two comparison stars (S_{10} and S_{11}) to calculate two object magnitudes ($m_{o|10}$ and $m_{o|11}$) based on the two comparison stars, and obtained the averaged value $m_o = \frac{1}{2}(m_{o|10} - m_{o|11})$ as the target magnitude at the same time. The deviation of magnitude difference $S_{10} - S_{11}$ from a certain night is the corresponding uncertainty for the whole observation night.

Our monitoring duration is from 2022 December 4 to 2023 January 28, and contains 2716 observations at the g , r , and i bands. At the g band, there are 929 observations, with the biggest variation $\Delta m_g = 0.945 \pm 0.048$ mag; see Figure 1 (the green dots). At the r band, there are 887 observations, with the biggest variation $\Delta m_r = 0.648 \pm 0.023$ mag; see Figure 1 (the red dots). At the i band, there are 900 observations, with the biggest variation $\Delta m_i = 0.945 \pm 0.051$ mag; see Figure 1 (the black dots).

The observations have been listed in Table 2.

3. Optical Variabilities

3.1. Intraday Optical Variabilities

3.1.1. Qualifying Criteria

Many methods can be used to constrain the intraday optical variability, such as the variability amplitude parameter (A_m), F -test, nested ANOVA, etc., which can be described as the following:

1. Variable amplitude parameter (A_m)

J. Heidt & S. J. Wagner (1996) pointed out this method,

$$A_m = 100 \times \sqrt{(m_x - m_n)^2 - \sigma_x^2 - \sigma_n^2} (\%),$$

where $m_x \pm \sigma_x$ was the maximum value and $m_n \pm \sigma_n$ was the minimum value. When $A_m > 7.5\%$, the source displayed variable properties.

2. F -test

J. A. De Diego (2010) introduced this method, which can be used to constrain the significance of a variation. This method can be described by $F = \frac{S_o^2}{S_t^2}$, where S_o^2 is the variance of the differential light-curve values of the object and S_t^2 is the variance of the differential light-curve values of the comparison stars.

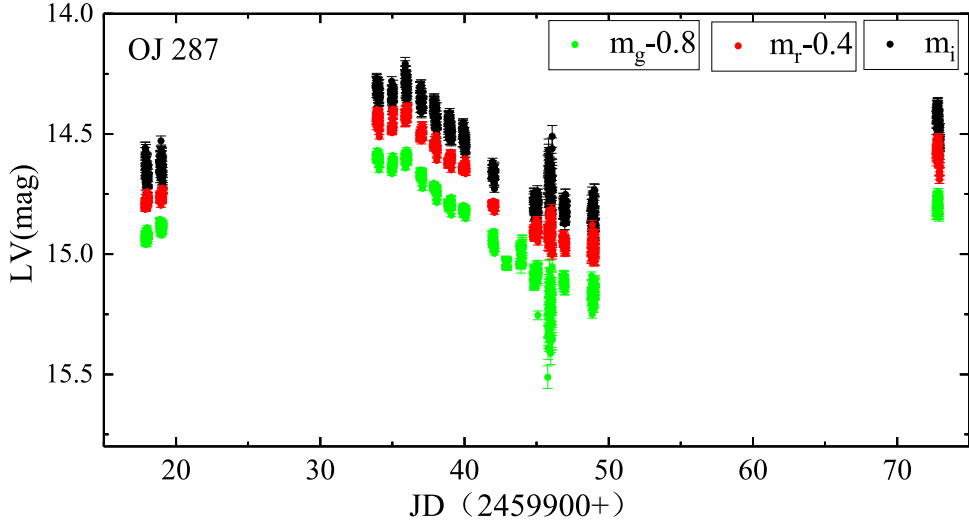


Figure 1. Multiband light curves of OJ 287 obtained with NGT. Black, red, and green points represent the i , r , and g bands, respectively.

Table 2
The Observations of OJ 287 at the g , r , and i Bands

g -JD (+2459900) (1)	m_g (mag) (2)	σ_g (mag) (3)	r -JD (+2459900) (4)	m_r (mag) (5)	σ_r (mag) (6)	i -JD (+2459900) (7)	m_i (mag) (8)	σ_i (mag) (9)
17.863	15.754	0.009	17.863	15.185	0.009	17.863	14.648	0.026
17.867	15.732	0.009	17.867	15.196	0.009	17.867	14.583	0.026
17.870	15.729	0.009	17.870	15.192	0.009	17.870	14.561	0.026
17.874	15.742	0.009	17.874	15.180	0.009	17.874	14.559	0.026
17.877	15.711	0.009	17.877	15.203	0.009	17.877	14.662	0.026
17.881	15.733	0.009	17.881	15.214	0.009	17.881	14.627	0.026
17.885	15.715	0.009	17.885	15.203	0.009	17.885	14.635	0.026
17.888	15.738	0.009	17.888	15.194	0.009	17.888	14.605	0.026
17.892	15.721	0.009	17.892	15.161	0.009	17.892	14.707	0.026
17.895	15.750	0.009	17.895	15.200	0.009	17.895	14.794	0.026
17.899	15.743	0.009	17.899	15.198	0.009	17.899	14.622	0.026

Note. Column (1): g -JD (+2459900). Column (2): m_g , in units of magnitude. Column (3): σ_g , uncertainty of m_g . Column (4): r -JD (+2459900). Column (5): m_r , in units of magnitude. Column (6): σ_r , uncertainty of m_r . Column (7): i -JD (+2459900). Column (8): m_i , in units of magnitude. Column (9): σ_i , uncertainty of m_i . (This table is available in its entirety in machine-readable form in the [online article](#).)

3. Nested ANOVA

The ANOVA test can compare the means of dispersion among the different groups of observations. The nested ANOVA test is an updated ANOVA test that can generate the different light curves of blazars based on several stars as the reference stars. The detailed introduction of this method is shown in J. A. De Diego et al. (2015).

For each intraday light-curve fit, the number of free parameters (ν_O and ν_C) is the same and equals $N - 1$. The degrees of freedom for each fit would instead be $\text{dof} = N - \nu_O$, where N is the number of data points in the light-curve segment.

In order to check the variable values of a target, we can compare the F value from the observations with the critical value, $F_{C(\nu_O, \nu_C)}$. An F -test can be determined within two significance levels (1% and 0.1%). This method is consistent with the 2.6σ and 3σ detections, respectively (e.g., J. A. De Diego 2010; J. H. Fan et al. 2017; D. Xiong et al. 2017).

3.1.2. Calculation Results

The intraday light curves exhibiting variability are shown in Figure 2 (g band), Figure 3 (r band), and Figure 4 (i band). Black points represent the source light curves, red points indicate the magnitude difference between comparisons “C10” and “C11,” and colored dashed lines mark the individual variability stages.

The analyzed results have been listed in Table 3 (g , r , and i bands).

In the g band, IDVs were detected on 10 of the 17 monitored nights, with variability timescales ranging from 0.68 to 6.95 hr and a maximum amplitude of $\Delta m = 0.459 \pm 0.066$ mag. In the r band, covering 15 nights, IDVs were detected on 10 nights, with timescales ranging from 0.51 to 3.98 hr and a largest variation of $\Delta m = 0.190 \pm 0.027$ mag. In the i band, also spanning 15 nights, IDVs occurred on six nights, with timescales from 0.51 to 4.23 hr and the most significant change reaching $\Delta m = 0.399 \pm 0.064$ mag.

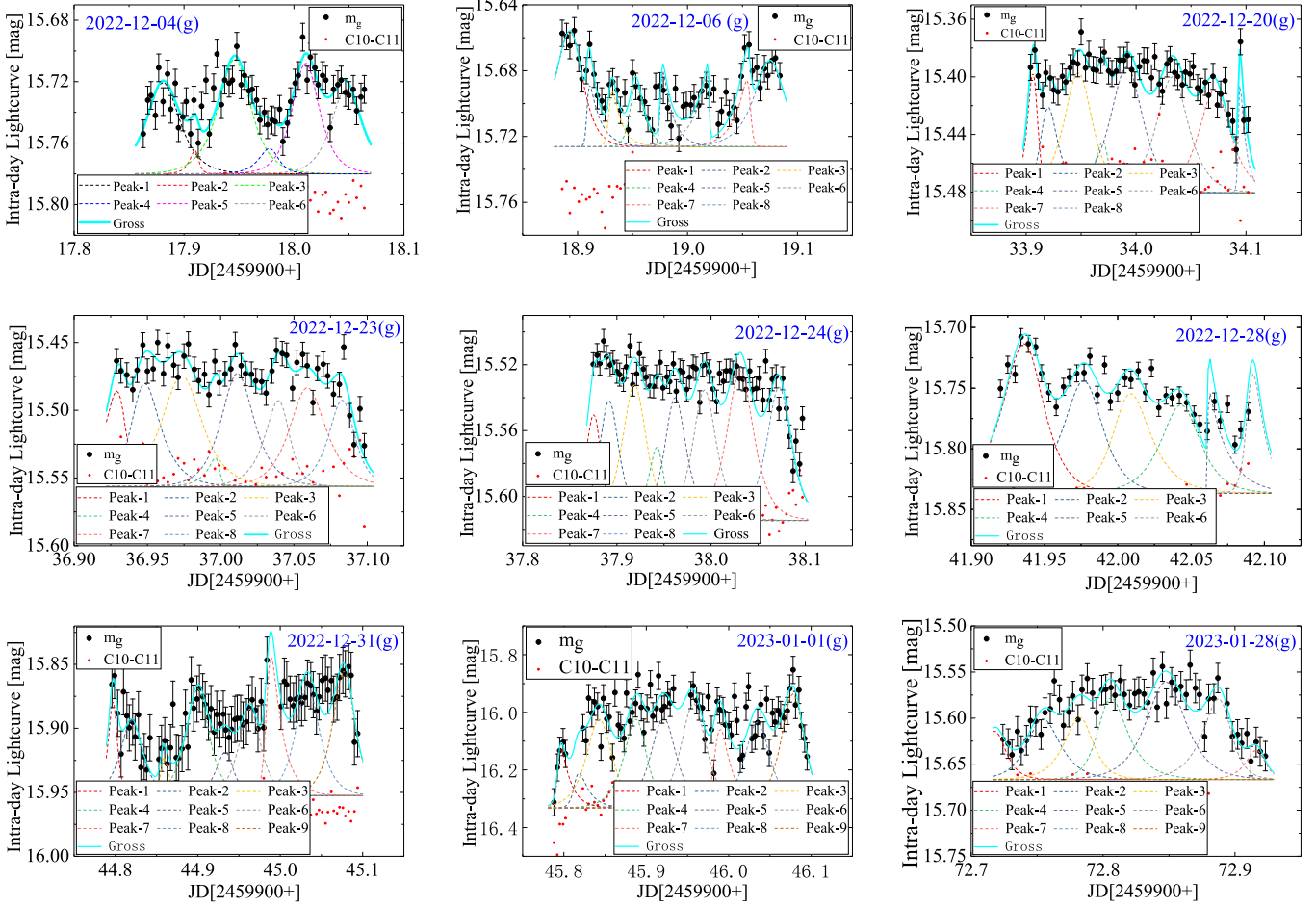


Figure 2. Intraday g -band optical variability. Black symbols trace the target light curve, red symbols show the magnitude difference between two comparison stars, and cyan curves mark the best-fit peaks.

3.1.3. Effects of Wavelength on the Results

We compare the effects of wavelength on Δm , ΔT , and VR (the ratio between Δm and ΔT).

3.1.3.1. Δm Distributions

Figure 5 shows the distributions of Δm . The left panel gives the cumulative functions; the right panel gives the number histograms. Gaussian fits yield for the g band: $\bar{\Delta m}_g = 0.055 \pm 0.005$ mag, $r = 0.53$, and $P = 2.95 \times 10^{-4}$; for the r band: $\bar{\Delta m}_r = 0.047 \pm 0.005$ mag, $r = 0.70$, and $P = 9.15 \times 10^{-7}$; and for the i band: $\bar{\Delta m}_i = 0.085 \pm 0.006$ mag, $r = 0.71$, and $P = 1.61 \times 10^{-7}$.

The i -band Δm distribution differs from those of the other two bands, whereas the g - and r -band distributions are mutually consistent.

3.1.3.2. ΔT Distributions

Figure 6 presents the distributions of variable timescales (ΔT): panel (a) shows the cumulative distributions, and panels (b)–(d) show the corresponding number histograms.

As shown in Figure 6(a), the ΔT distribution in the i band is significantly shorter than those in the g and r bands. The ΔT data from the g band can be categorized into four distinct components (Figure 6(b)), each fitted with Gaussian functions yielding a correlation coefficient of $r = 0.76$, with $P = 7.49 \times 10^{-6}$. The

corresponding mean values for four components are $\bar{\Delta T}_1 = 0.44 \pm 0.43$ hr, $\bar{\Delta T}_2 = 1.35 \pm 1.26$ hr, $\bar{\Delta T}_3 = 3.09 \pm 0.72$ hr, and $\bar{\Delta T}_4 = 6.45 \pm 0.77$ hr, respectively.

In the r band (Figure 6(c)) the ΔT histogram is resolved into two Gaussians ($r = 0.71$, $P = 3.75 \times 10^{-7}$) with means $\bar{\Delta T}_1 = 0.42 \pm 0.04$ hr and $\bar{\Delta T}_2 = 1.27 \pm 0.89$ hr. An identical two-component fit to the i -band data (Figure 6(d)) yields an even higher correlation ($r = 0.78$, $P = 8.58 \times 10^{-8}$) and mean timescales $\bar{\Delta T}_1 = 0.36 \pm 0.09$ hr and $\bar{\Delta T}_2 = 0.81 \pm 1.41$ hr.

3.1.3.3. Variable Rate Distributions

The variable rate (VR) distributions are shown in Figure 7, where the black lines stand for the g band, the red lines stand for the r band, and the blue lines stand for the i band.

In the g band, the VR distribution is resolved into three components with mean values $\bar{VR}_1 = -1.28 \pm 0.22$ mag hr^{-1} , $\bar{VR}_2 = -0.91 \pm 0.67$ mag hr^{-1} , and $\bar{VR}_3 = -0.31 \pm 0.08$ mag hr^{-1} . The correlation coefficient $r = 0.78$ and $P = 1.89 \times 10^{-5}$.

In the r band, the mean value is $\bar{VR} = -1.16 \pm 0.03$ mag hr^{-1} ($r = 0.88$, $P = 5.07 \times 10^{-12}$); in the i band, it is $\bar{VR} = -0.79 \pm 0.03$ mag hr^{-1} ($r = 0.84$, $P = 7.03 \times 10^{-11}$).

Most of the VR from the g band displays a consistent distribution with the values from the r band. But the VR from

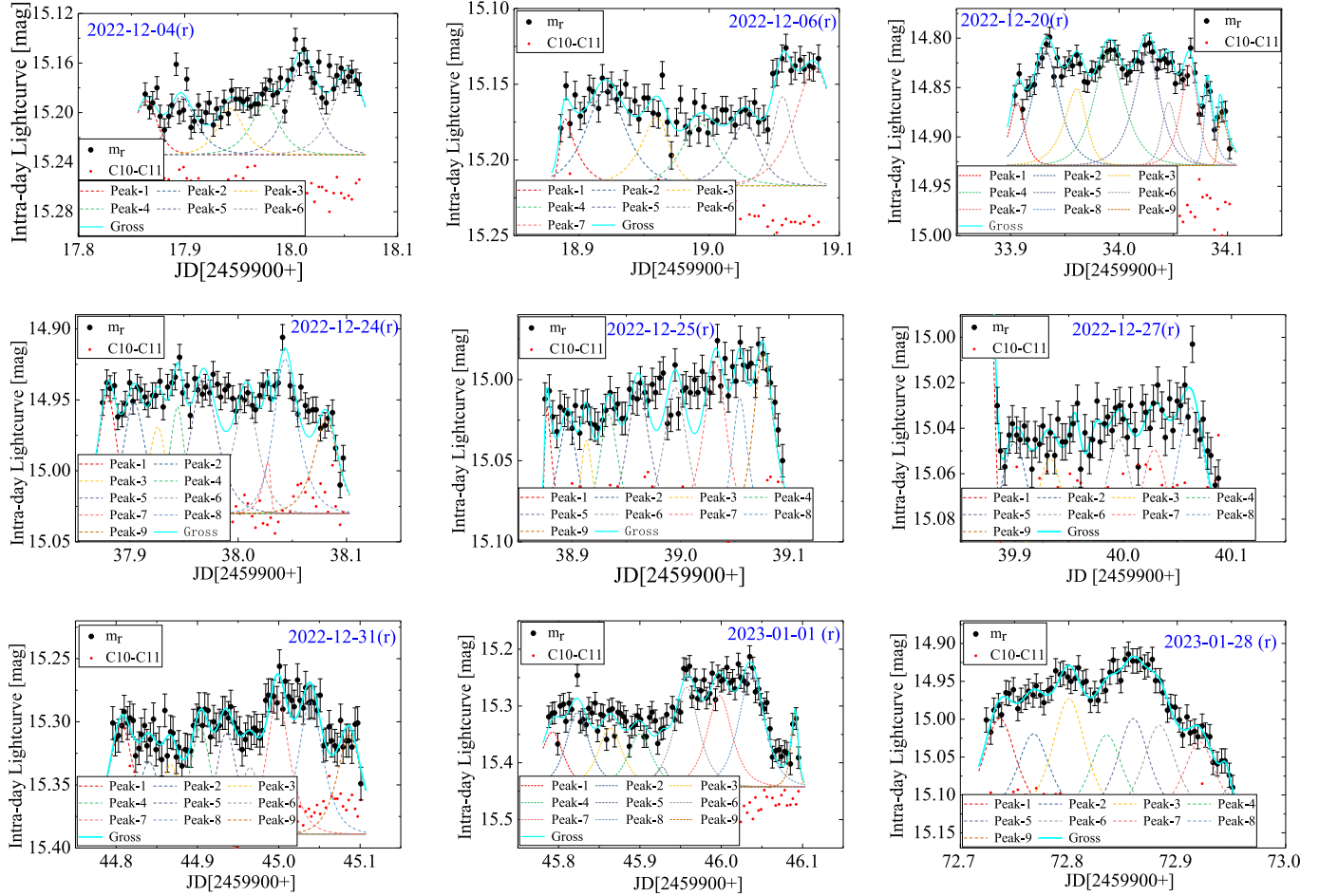


Figure 3. Intraday r -band optical variability. Black symbols trace the target light curve, red symbols show the magnitude difference between two comparison stars, and cyan curves mark the best-fit peaks.

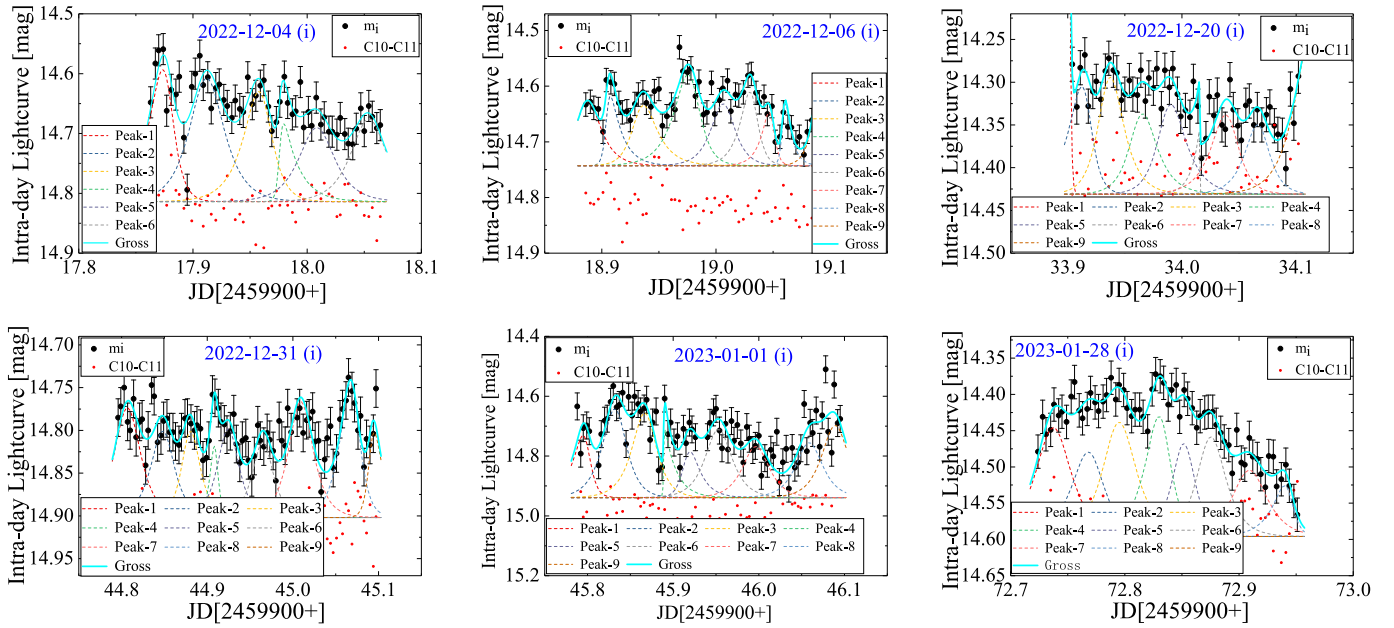


Figure 4. Intraday i -band optical variability. Black symbols trace the target light curve, red symbols show the magnitude difference between two comparison stars, and cyan curves mark the best-fit peaks.

Table 3
The IDV Results of OJ 287 at the *g*, *r*, and *i* Bands

Band	Date	<i>N</i>	<i>Am</i>	<i>F</i> ₁	<i>F</i> ₂	\bar{F}	Nested ANOVA (F)	<i>F</i> ₍₉₉₎ ^c	<i>F</i> _(99.9) ^c	Note	ΔT (hr)	$\Delta m \pm \sigma$ (mag)	VR (mag hr ⁻¹)	$\frac{\Delta m}{\sigma}$
(1)	(2)	(3)	(4)	(5)	(6)	(7)	(8)	(9)	(10)	(11)	(12)	(13)	(14)	(15)
<i>g</i>	2022/12/04	58	6.80	2.04	1.66	1.85	4.73	1.87	2.30	V	2.29	0.069 ± 0.013	-1.52	5.44
	2022/12/06	57	6.45	1.17	0.74	0.95	9.97	1.88	2.32	V	2.29	0.066 ± 0.011	-1.54	5.79
	2022/12/20	57	8.08	1.26	1.35	1.30	4.25	1.88	2.32	V	3.38	0.082 ± 0.013	-1.62	6.43
	2022/12/21	32	7.43	2.56	1.10	1.83	16.45	2.35	3.15	V	1.52	0.075 ± 0.011	-1.31	6.65
	2022/12/22	49	7.20	3.85	9.66	6.76	1.44	1.98	2.49	N
	2022/12/23	49	7.51	2.18	3.09	2.64	3.58	1.98	2.49	V	1.44	0.070 ± 0.013	-1.31	5.53
	2022/12/24	64	7.84	1.20	1.17	1.18	12.37	1.81	2.21	V	0.68	0.067 ± 0.010	-1.01	6.69
	2022/12/25	63	7.30	1.20	1.50	1.35	0.49	1.82	2.22	N
	2022/12/27	59	5.45	2.27	2.34	2.31	1.59	1.86	2.28	N
	2022/12/28	39	9.02	3.40	3.40	3.40	7.81	2.16	2.80	V	3.48	0.089 ± 0.010	-1.59	8.97
	2022/12/29	27	0.86	1.13	0.94	1.03	1.77	2.55	3.53	N
	2022/12/30	53	6.72	0.41	0.04	0.22	15.68	1.92	2.40	N
	2022/12/31	80	8.44	3.54	3.10	3.32	8.78	1.70	2.02	V	6.21	0.088 ± 0.025	-1.85	3.52
	2023/01/01	78	45.45	2.37	3.51	2.94	4.15	1.71	2.04	V	6.95	0.459 ± 0.066	-1.90	6.95
	2023/01/02	31	6.68	10.47	1.98	6.23	4.58	2.39	3.22	N
	2023/01/04	76	15.82	1.08	1.06	1.07	2.70	1.72	2.06	N
	2023/01/28	56	10.19	3.92	0.69	2.31	15.00	1.89	2.34	V	1.11	0.104 ± 0.023	-1.03	4.52
<i>r</i>	2022/12/04	58	7.24	1.98	3.02	2.50	8.33	1.87	2.30	V	2.96	0.073 ± 0.013	-1.61	5.77
	2022/12/06	57	7.00	2.24	2.16	2.20	10.83	1.88	2.32	V	2.11	0.071 ± 0.012	-1.47	5.59
	2022/12/20	57	11.15	1.21	1.30	1.26	13.00	1.88	2.32	V	3.98	0.112 ± 0.014	-1.55	7.95
	2022/12/21	31	9.74	3.00	8.29	5.65	56.81	2.39	3.22	V	1.61	0.098 ± 0.013	-1.21	7.72
	2022/12/22	49	6.88	1.78	5.13	3.46	2.04	1.98	2.49	N
	2022/12/23	49	6.60	1.02	1.69	1.36	5.16	1.98	2.49	N
	2022/12/24	64	10.30	1.07	1.09	1.08	9.06	1.81	2.21	V	1.61	0.072 ± 0.013	-1.35	5.66
	2022/12/25	63	7.26	1.07	1.50	1.29	6.46	1.82	2.22	V	1.44	0.074 ± 0.014	-1.29	5.23
	2022/12/27	59	6.14	2.00	2.98	2.49	2.94	1.86	2.28	V	0.51	0.062 ± 0.011	-0.91	5.52
	2022/12/28	39	4.44	1.23	0.97	1.10	1.53	2.16	2.80	N
	2022/12/31	87	9.06	1.03	1.01	1.02	1.53	1.66	1.96	V	2.38	0.092 ± 0.018	-1.41	5.11
	2023/01/01	86	18.76	2.55	3.51	3.03	11.13	1.66	1.97	V	1.19	0.190 ± 0.027	-0.80	7.04
	2023/01/02	47	8.35	1.62	1.68	1.65	4.85	2.01	2.54	N
	2023/01/04	76	15.18	1.61	2.12	1.87	4.42	1.72	2.06	N
	2023/01/28	65	17.51	3.33	2.95	3.14	17.48	1.80	2.19	V	2.30	0.177 ± 0.023	-1.11	7.70
<i>i</i>	2022/12/04	58	23.19	1.06	0.88	0.97	3.70	1.87	2.30	V	0.51	0.235 ± 0.036	-0.34	6.39
	2022/12/06	57	19.15	3.13	3.93	3.53	5.35	1.88	2.32	V	2.62	0.194 ± 0.029	-1.13	6.53
	2022/12/20	57	12.92	1.22	1.24	1.23	6.95	1.88	2.32	V	4.23	0.132 ± 0.028	-1.51	4.68
	2022/12/21	32	11.46	6.10	1.44	3.77	0.47	2.35	3.15	N
	2022/12/22	49	14.69	2.05	0.72	1.38	4.88	1.98	2.49	N
	2022/12/23	49	11.02	3.86	1.75	2.81	5.47	1.98	2.49	N
	2022/12/24	64	13.63	1.12	1.10	1.11	35.36	1.81	2.21	N
	2022/12/25	63	11.87	1.97	1.89	1.93	8.44	1.82	2.22	N
	2022/12/27	59	12.84	1.93	1.14	1.53	11.71	1.86	2.28	N
	2022/12/28	39	10.96	3.85	2.10	2.98	1.37	2.16	2.80	N
	2022/12/31	85	13.07	0.96	1.02	0.99	2.46	1.67	1.98	V	0.77	0.134 ± 0.031	-0.76	4.32

Table 3
(Continued)

Band	Date	N	Am	F_1	F_2	\bar{F}	Nested ANOVA (F)	$F_{(99)}^c$	$F_{(99.9)}^c$	Note	ΔT (hr)	$\Delta m \pm \sigma$ (mag)	VR (mag hr $^{-1}$)	$\frac{\Delta m}{\sigma}$
(1)	(2)	(3)	(4)	(5)	(6)	(7)	(8)	(9)	(10)	(11)	(12)	(13)	(14)	(15)
	2023/01/01	83	39.42	1.45	0.96	1.21	4.81	1.68	2.00	V	1.02	0.399 ± 0.064	-0.41	6.23
	2023/01/02	54	11.81	1.32	3.05	2.19	42.38	1.91	2.38	N
	2023/01/04	76	19.74	2.70	1.53	2.11	1.08	1.72	2.06	N
	2023/01/28	73	22.17	2.75	3.33	3.04	3.09	1.74	2.09	V	3.06	0.224 ± 0.033	-1.14	6.79

Note. Column (1): band. Column (2): date. Column (3): the number of observations, N . Column (4): the variability amplitude parameter, Am . Column (5): F -test from the first comparison, F_1 . Column (6): F -test from the second comparison, F_2 . Column (7): averaged values of F_1 and F_1 , \bar{F} . Column (8): nested ANOVA (F value). Column (9): 1% significance level, $F_{(99)}^c$. Column (10): 0.1% significance level, $F_{(99.9)}^c$. Column (11): V: variance, N: no variance. Column (12): variable timescales, ΔT , in hours. Column (13): the variable value and error, $\Delta m \pm \sigma$, in magnitude. Column (14): the variable rate, $\frac{\Delta m}{\Delta T}$, in mag hr $^{-1}$. Column (15): ratio between the variable value and error, $\frac{\Delta m}{\sigma}$. When the analyzed results satisfy $Am > 7.5\%$, $F_{1,2} > F_{99}^c$, or $F_{1,2} > F_{99.9}^c$, the IDVs can be accepted.

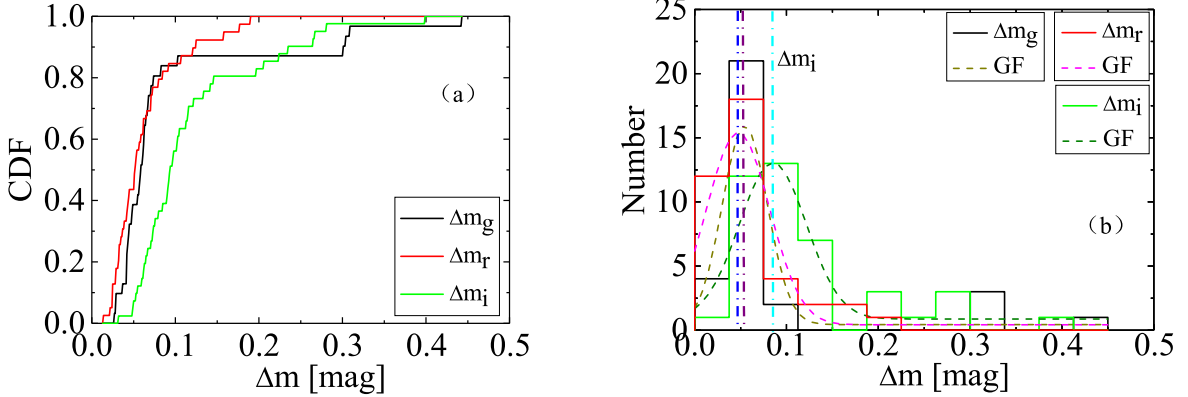


Figure 5. The distributions of the variable values (Δm). The black, red, and green lines stand for the variable values from the g band, r band, and i band, respectively. The left panel shows cumulation relations and the right panel shows for number distributions, where the dotted lines stand for Gaussian fitting (GF).

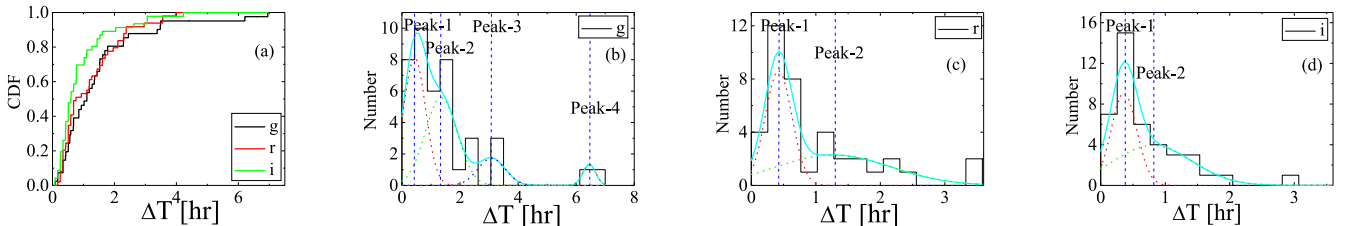


Figure 6. The distributions of variable timescales (ΔT), where panel (a) shows cumulation relations, with the black, red, and green lines standing for the g , r , and i bands. The three panels (b), (c), and (d) show the number distribution, with the cyan lines showing the combination of individual Gaussian fitting (GF).

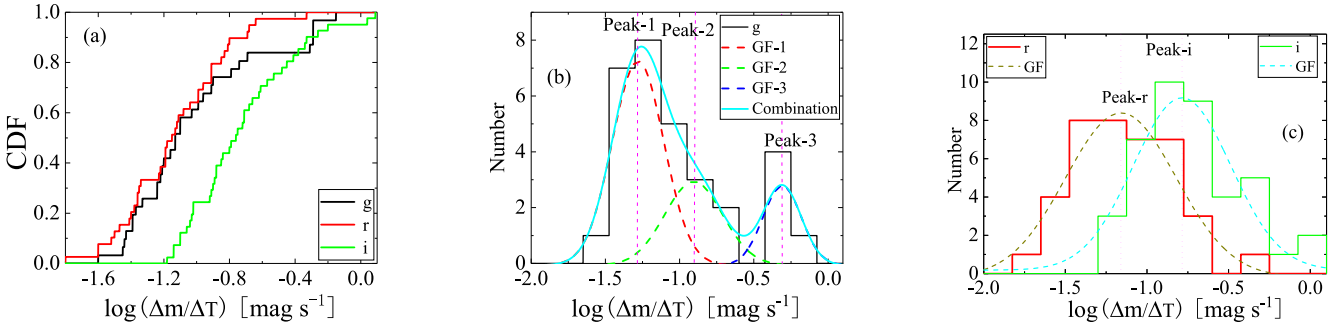


Figure 7. The distributions of the variable rate ($\frac{\Delta m}{\Delta T}$), where the black lines stand for the g band, the red lines stand for the r band, and the green lines stand for the i band. The left panel shows cumulation relations. The right two panels show for number distribution, where the colored dashed lines stand for the Gaussian fitting (GF).

the i band is significantly stronger than the values from the g and r bands.

3.2. Contour Fitting of Intraday Light Curves

3.2.1. Method

In order to analyze the contour of an intraday light curve, we use a multi-Gaussian fitting function, which can be introduced as the following:

$$y = y_0 + 2k_1(e^{(T'_1-t)/\Delta T'_{b1}} + e^{(t-T'_1)/\Delta T'_{d1}})^{-1} + 2k_2(e^{(T'_2-t)/\Delta T'_{b2}} + e^{(t-T'_2)/\Delta T'_{d2}})^{-1} + \dots \quad (2)$$

where T'_i ($i = 1, 2, 3, \dots$) is the time of the i th minipeak, k_i is its amplitude, and $\Delta T'_{b|i}$ and $\Delta T'_{d|i}$ are the brightening and dimming timescales, respectively. N is set equal to the number of minipeaks identified by eye in the light curve.

3.2.2. Calculation Results

The fitting curves are displayed in Figure 2 (g band), Figure 3 (r band), and Figure 4 (i band), where the black dots stand for the light curves, the colored lines stand for the fitting of every peak, and the cyan lines stand for the combination of every peak. We list the fitting parameters in Table 4 (g band), Table 5 (r band), and Table 6 (i band).

3.2.3. Effects of Wavelength on the Peak Locations

The time intervals between adjacent peaks, $\Delta T'$, were calculated to characterize their distribution, shown in the left panel of Figure 8. The black, green, and red lines correspond to the g , r , and i bands respectively; dashed curves mark the Gaussian fits.

Statistical analysis reveals:

Table 4
The Fitting Results of OJ 287 Based on the Multiorder Power-law Function at the g Band

Date (1)	k (2)	$\Delta T'_b$ (3) (minutes)	T' (4) (minutes)	$\Delta T'_d$ (5) (minutes)	k (2)	$\Delta T'_b$ (3) (minutes)	T' (4) (minutes)	$\Delta T'_d$ (5) (minutes)	k (2)	$\Delta T'_b$ (3) (minutes)	T' (4) (minutes)	$\Delta T'_d$ (5) (minutes)	k (2)	$\Delta T'_b$ (3) (minutes)	T' (4) (minutes)	$\Delta T'_d$ (5) (minutes)
2022/12/4	0.06	19.33	25.81	19.41	0.01	7.64	69.37	3.49	0.07	19.63	120.23	18.46	0.02	13.77	167.21	9.48
	0.07	15.16	211.89	16.46	0.06	16.78	264.47	18.97
2022/12/6	0.07	19.81	13.21	13.06	0.03	1.48	32.88	14.89	0.03	2.41	62.41	11.94	0.04	5.43	94.17	10.72
	0.03	1.45	128.92	13.37	0.03	18.53	192.68	0.64	0.03	16.92	245.83	2.15	0.05	19.62	273.98	16.05
2022/12/20	0.08	8.00	4.87	4.53	0.06	7.96	20.65	13.35	0.08	17.44	63.27	16.10	0.03	12.26	97.93	4.82
	0.09	19.93	126.74	18.54	0.08	18.96	185.81	18.77	0.07	18.69	241.25	18.52	0.05	1.07	272.51	8.17
2022/12/23	0.06	15.10	4.30	5.69	0.07	10.57	25.20	15.69	0.08	17.80	64.19	17.45	0.02	10.63	99.90	2.01
	0.08	13.70	117.81	15.31	0.06	13.64	161.40	8.44	0.07	14.98	186.47	16.87	0.06	12.58	222.67	10.35
2022/12/24	0.06	14.02	3.33	8.62	0.07	13.14	23.64	14.02	0.08	16.49	62.97	16.34	0.04	13.46	99.96	7.85
	0.07	14.12	124.44	15.54	0.08	15.86	169.42	16.71	0.09	18.12	224.29	18.51	0.08	17.42	284.59	15.86
2022/12/28	0.12	20.00	25.00	16.11	0.09	18.99	83.33	15.71	0.08	13.74	124.83	19.91	0.07	18.05	178.06	16.41
	0.05	0.36	203.56	19.54	0.09	4.12	245.00	11.64
2022/12/31	0.07	8.41	3.21	5.77	0.06	17.84	35.01	16.65	0.03	3.55	87.75	10.07	0.08	18.55	150.56	17.03
	0.03	15.20	199.04	12.25	0.07	17.16	241.25	16.49	0.09	4.79	272.41	19.90	0.09	18.14	340.85	19.30
	0.10	18.10	406.12	16.13
2023/1/1	0.16	3.25	7.98	17.04	0.10	5.35	38.66	18.51	0.31	19.99	79.25	19.84	0.31	19.86	145.02	15.77
	0.31	20.00	191.28	19.94	0.36	19.94	243.79	20.00	0.24	6.76	285.00	19.97	0.30	19.85	355.16	19.96
	0.40	19.94	418.99	16.81
2023/1/28	0.05	12.10	-8.11	10.42	0.07	14.56	42.30	17.69	0.07	16.04	85.61	12.17	0.09	10.83	114.28	19.02
	0.11	19.16	177.62	19.76	0.08	17.83	238.81	10.41	0.03	11.57	278.65	7.56	5.00	5.02	360.00	5.00
	5.00	5.00	410.00	5.00

Note. Column (1): date. Column (2): the fitting results, k . Column (3): the brightening timescales. Column (4): the peak time. Column (5): the dimming timescales.

Table 5
The Fitting Results of OJ 287 Based on the Multiorder Power-law Function at the r Band

Date (1)	k (2)	$\Delta T'_b$ (3) (minutes)	T' (4) (minutes)	$\Delta T'_d$ (5) (minutes)	k (2)	$\Delta T'_b$ (3) (minutes)	T' (4) (minutes)	$\Delta T'_d$ (5) (minutes)	k (2)	$\Delta T'_b$ (3) (minutes)	T' (4) (minutes)	$\Delta T'_d$ (5) (minutes)	k (2)	$\Delta T'_b$ (3) (minutes)	T' (4) (minutes)	$\Delta T'_d$ (5) (minutes)	
2022/12/4	0.06	19.33	25.81	19.41	0.01	7.64	69.37	3.49	0.07	19.63	120.23	18.46	0.02	13.77	167.21	9.48	
	0.07	15.16	211.89	16.46	0.06	16.78	264.47	18.97	
2022/12/6	0.07	19.81	13.21	13.06	0.03	1.48	32.88	14.89	0.03	2.41	62.41	11.94	0.04	5.43	94.17	10.72	
	0.03	1.45	128.92	13.37	0.03	18.53	192.68	0.64	0.03	16.92	245.83	2.15	0.05	19.62	273.98	16.05	
2022/12/20	0.08	8.00	4.87	4.53	0.06	7.96	20.65	13.35	0.08	17.44	63.27	16.10	0.03	12.26	97.93	4.82	
	0.09	19.93	126.74	18.54	0.08	18.96	185.81	18.77	0.07	18.69	241.25	18.52	0.05	1.07	272.51	8.17	
2022/12/23	0.06	15.10	4.30	5.69	0.07	10.57	25.20	15.69	0.08	17.80	64.19	17.45	0.02	10.63	99.90	2.01	
	0.08	13.70	117.81	15.31	0.06	13.64	161.40	8.44	0.07	14.98	186.47	16.87	0.06	12.58	222.67	10.35	
2022/12/24	0.06	14.02	3.33	8.62	0.07	13.14	23.64	14.02	0.08	16.49	62.97	16.34	0.04	13.46	99.96	7.85	
	0.07	14.12	124.44	15.54	0.08	15.86	169.42	16.71	0.09	18.12	224.29	18.51	0.08	17.42	284.59	15.86	
10	2022/12/28	0.12	20.00	25.00	16.11	0.09	18.99	83.33	15.71	0.08	13.74	124.83	19.91	0.07	18.05	178.06	16.41
	0.05	0.36	203.56	19.54	0.09	4.12	245.00	11.64	
2022/12/31	0.07	8.41	3.21	5.77	0.06	17.84	35.01	16.65	0.03	3.55	87.75	10.07	0.08	18.55	150.56	17.03	
	0.03	15.20	199.04	12.25	0.07	17.16	241.25	16.49	0.09	4.79	272.41	19.90	0.09	18.14	340.85	19.30	
	0.10	18.10	406.12	16.13	
2023/1/1	0.16	3.25	7.98	17.04	0.10	5.35	38.66	18.51	0.31	19.99	79.25	19.84	0.31	19.86	145.02	15.77	
	0.31	20.00	191.28	19.94	0.36	19.94	243.79	20.00	0.24	6.76	285.00	19.97	0.30	19.85	355.16	19.96	
	0.40	19.94	418.99	16.81	
2023/1/28	0.05	12.10	-8.11	10.42	0.07	14.56	42.30	17.69	0.07	16.04	85.61	12.17	0.09	10.83	114.28	19.02	
	0.11	19.16	177.62	19.76	0.08	17.83	238.81	10.41	0.03	11.57	278.65	7.56	5.00	5.02	360.00	5.00	
	5.00	5.00	410.00	5.00	

Note. Column (1): date. Column (2): the fitting results, k . Column (3): the brightening timescales. Column (4): the peak time. Column (5): the dimming timescales.

Table 6
The Fitting Results of OJ 287 Based on the Multiorder Power-law Function at the *i* Band

Date (1)	k (2)	$\Delta T'_b$ (3) (minutes)	T' (4) (minutes)	$\Delta T'_d$ (5) (minutes)	k (2)	$\Delta T'_b$ (3) (minutes)	T' (4) (minutes)	$\Delta T'_d$ (5) (minutes)	k (2)	$\Delta T'_b$ (3) (minutes)	T' (4) (minutes)	$\Delta T'_d$ (5) (minutes)	k (2)	$\Delta T'_b$ (3) (minutes)	T' (4) (minutes)	$\Delta T'_d$ (5) (minutes)
2022/12/4	0.21	20.00	20.00	9.32	0.21	19.05	70.00	20.00	0.18	20.00	140.00	12.47	0.09	2.55	163.12	20.00
	0.12	20.00	209.36	20.00	0.14	20.00	275.00	20.00
2022/12/6	0.12	12.63	0.69	15.82	0.10	2.98	26.94	15.36	0.10	10.51	68.99	18.47	0.16	18.42	132.30	11.17
	0.11	14.20	173.96	12.72	0.13	12.94	209.62	7.30	0.09	10.98	234.05	4.35	0.10	2.42	249.45	8.32
	0.74	8.61	310.00	18.18
2022/12/20	0.62	18.88	-4.74	1.40	0.12	19.55	16.98	8.40	0.14	12.55	46.09	16.42	0.09	13.41	86.29	17.99
	0.10	13.04	121.22	19.38	0.04	10.79	161.25	0.15	0.09	18.39	196.16	12.72	0.08	15.70	235.44	12.26
	0.20	19.34	303.69	19.65
2022/12/31	0.13	19.99	15.77	19.52	0.10	18.82	75.97	16.95	0.10	12.63	120.36	15.39	0.08	7.58	162.94	4.97
	0.10	16.19	185.19	15.85	0.09	16.06	243.77	15.15	0.14	18.03	306.74	18.65	0.15	17.86	393.82	11.70
	0.09	6.20	426.16	16.51
2023/1/1	0.19	20.00	15.00	8.05	0.30	20.00	65.00	16.35	0.28	20.00	115.00	16.76	0.13	0.61	145.26	19.85
	0.14	8.93	185.42	18.44	0.23	19.97	237.50	20.00	0.17	20.00	300.13	20.00	0.18	20.00	390.00	20.00
	0.24	19.99	433.68	20.00
2023/1/28	0.15	20.00	19.32	20.00	0.12	20.00	65.00	16.68	0.16	18.12	101.52	19.68	0.16	18.57	155.99	11.37
	0.13	13.84	184.50	12.31	0.14	15.67	217.33	17.12	0.09	19.50	266.36	19.75	0.06	18.38	315.78	6.77
	5.00	5.00	430.00	5.00

Note. Column (1): date. Column (2): the fitting results, k . Column (3): the brightening timescales. Column (4): the peak time. Column (5): the dimming timescales.

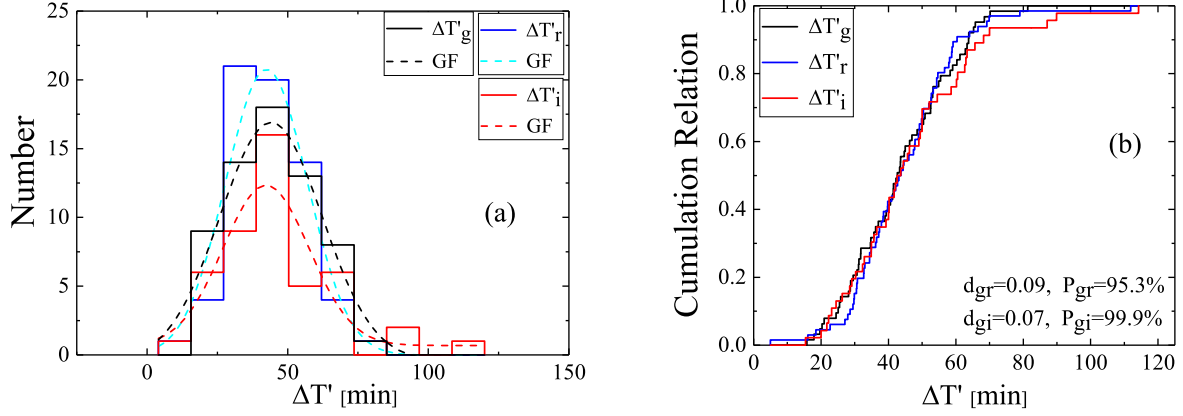


Figure 8. The distributions of the time differences between the adjacent peaks. The black, red, and green lines stand for the g , r , and i bands, respectively. The dashed lines stand for the Gaussian fitting (GF).

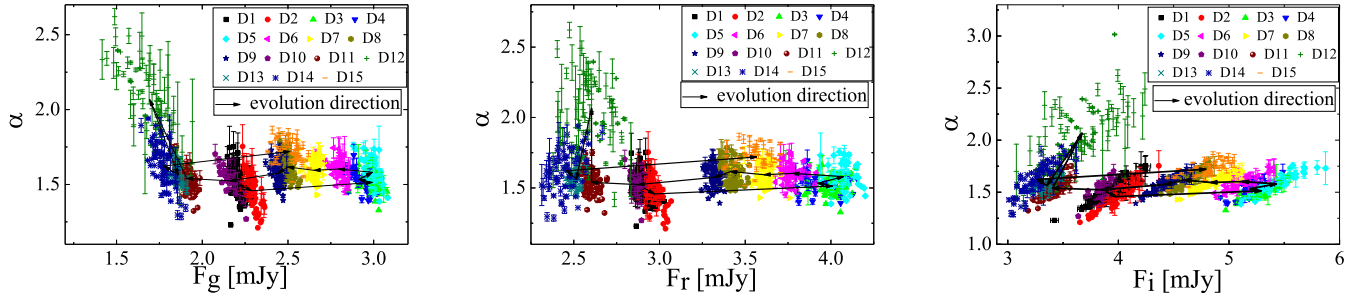


Figure 9. The relations between the flux densities (F_{gr}) and spectral indices (α). From the left to right, the panels stand for F_g versus α , F_r versus α and F_i versus α , individually. The arrow lines represent the evolution direction. D1: 2022/12/04, D2: 2022/12/06, D3: 2022/12/20, D4: 2022/12/21, D5: 2022/12/22, D6: 2022/12/23, D7: 2022/12/24, D8: 2022/12/25, D9: 2022/12/27, D10: 2022/12/28, D11: 2022/12/31, D12: 2023/01/01, D13: 2023/01/03, D14: 2023/01/04, and D15: 2023/01/28.

1. g band: central value $\Delta T'_{g|6} = 44.10 \pm 1.60$ minutes ($r = 0.88$, $P = 1.39 \times 10^{-5}$),
2. r band: $\Delta T'_{r|c} = 42.47 \pm 1.68$ minutes ($r = 0.83$, $P = 6.02 \times 10^{-8}$),
3. i band: $\Delta T'_{i|c} = 42.31 \pm 2.31$ minutes ($r = 0.74$, $P = 9.29 \times 10^{-7}$).

The combined value, $\bar{\Delta T'}_{\text{gr}|c} = 42.96 \pm 0.99$ minutes, is consistent across bands within the uncertainties, indicating frequency-independent characteristic.

We used a Kolmogorov–Smirnov test to compare the ΔT distributions across bands (right panel of Figure 8). The maximum deviations are $d_{gr} = 0.09$ and $d_{gi} = 0.07$, with probabilities $P_{gr} = 95.3\%$ and $P_{gi} = 99.9\%$ that the samples are drawn from the same parent distribution. These results confirm that ΔT is independent of frequency.

3.3. Relations between the Flux Densities and Spectral Indices

The spectral indices α were derived from the contemporaneous g -, r -, and i -band flux densities (F_{gr}) as follows.

1. Galactic-extinction corrections were applied using the NED³ values, $A_g = 0.093$ mag, $A_r = 0.064$ mag, and $A_i = 0.048$ mag.
2. Dereddened magnitudes were converted to flux densities F_ν at the effective frequencies $\nu_g = 6.17 \times 10^{14}$ Hz, $\nu_r = 4.77 \times 10^{14}$ Hz, and $\nu_i = 3.89 \times 10^{14}$ Hz.

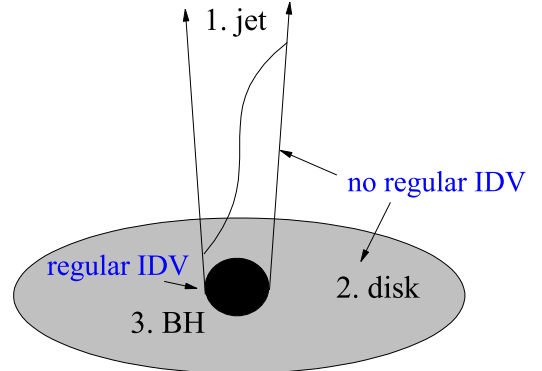


Figure 10. The origin model of the IDV phenomenon of OJ 287.

3. A power law $F_\nu \propto \nu^{-\alpha}$ was fitted to the three simultaneous flux densities to obtain α .

The distributions between F_{gr} and α have been shown in Figure 9, where the panels from left to right represent the relationships in the g , r , and i bands, respectively.

1. In the g band, when the flux is below 2 mJy, a consistent BWB behavior is observed between F_g and α across the monitored nights. Over the entire observation period, both F_g and α exhibit a clear time-dependent evolutionary trend, except on 2023 January 1. On this specific date, despite the relatively low flux values, the spectral index α remains exceptionally soft.

³ <http://ned.ipac.caltech.edu>

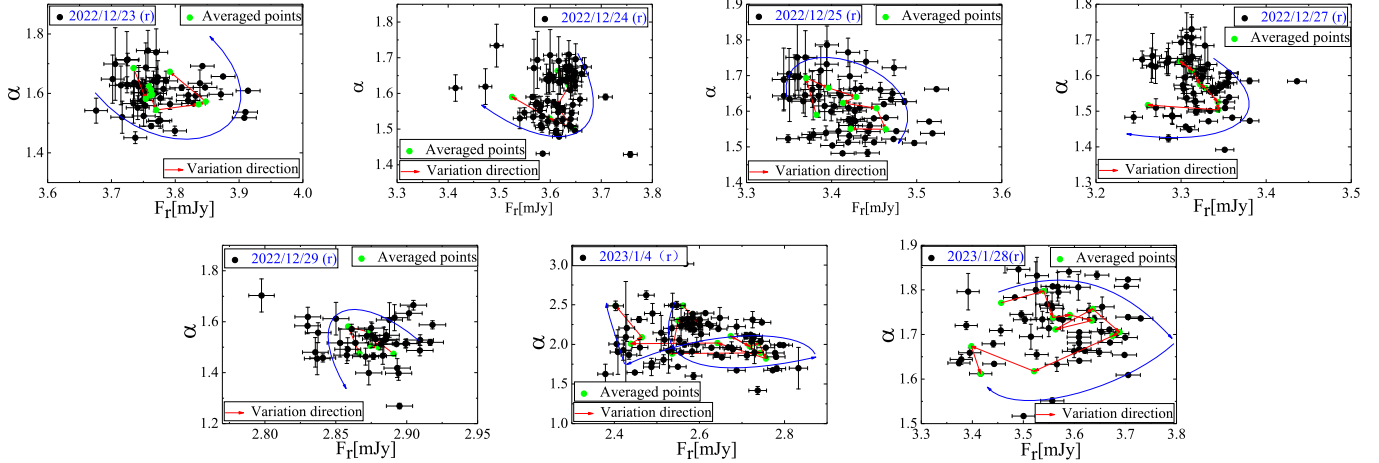


Figure 11. The relations between the flux densities (F_r) and spectral indices (α) on seven nights. The black dots stand for F_r versus α , the green dots stand for the averaged values, and the blue arrow lines display the evolution direction.

2. In the r band, the relationship varies: F_r and α show BWB behavior on some nights but transition to RWB behavior on others.
3. In the i band, an RWB trend dominates uniformly throughout all observations.

Overall, there is no evident correlation between flux and spectral index in any band across all monitored nights, with the sole exception of 2023 January 1 and 2024 January 4, when the lowest fluxes were recorded.

4. Discussion and Conclusion

4.1. The Origin of Intraday Optical Variabilities

OJ 287 is an exceptionally active source whose IDV has been reported frequently and exhibits puzzling, complex patterns. Quasiperiodic IDVs have been claimed by E. Valtaoja et al. (1985), W. M. Kinzel et al. (1988), and Y. H. Yuan et al. (2021), whereas A. C. Gupta et al. (2024), D. T. Zhou et al. (2024), and others find no evidence for periodicity.

During our observations, IDV occurrence rates were as follows:

1. 58.8% (10/17) in the g band,
2. 66.7% (10/15) in the r band,
3. 40% (6/15) in the i band.

Our characterization of the IDV yields three parameters: the amplitude Δm , the timescale ΔT , and their ratio $VR = \Delta m / \Delta T$. The distributions of Δm , ΔT , and VR measured in the g and r bands are mutually consistent, but differ markedly from those obtained in the i band, revealing a clear frequency dependence.

When we availed a multi-Gaussian function to fit the intraday light curves, we obtained the peak time (T') and calculated the time difference ($\Delta T'$). We compared $\Delta T'$ from three bands, but found that $\Delta T'$ are not frequency dependent.

In this study we identified two distinct classes of IDV. The first exhibits a regular, repeatable structure and is frequency independent; the second lacks any regular pattern and displays pronounced frequency-dependent behavior.

To interpret these findings we propose the scenario sketched in Figure 10:

1. The observed IDV is produced by emission from three distinct regions: the central black hole, the accretion disk, and the jet.
2. Variability tied to the black hole itself is regular (possibly periodic).
3. Fluctuations arising in the disk and jet are irregular and give rise to the frequency-dependent component.

4.2. The Regular Intraday Variabilities

Intraday periodic oscillations belong to microvariability and have been detected in several sources. For OJ 287, E. Valtaoja et al. (1985) measured a radio period of ~ 15.7 minutes, while W. M. Kinzel et al. (1988) found $\sim 66.9 \pm 4.1$ minutes at 7 mm.

In this work, the central value of the time difference between the adjacent peak is $\Delta T_{\text{grlc}}^{\bar{T}} = 42.96 \pm 0.99$ minutes. Considering the innermost part of the blazar near the central black hole, J. H. Fan et al. (2019) proposed the dependency relationship between the innermost stable orbit period (P) and the mass of the central black hole (M):

1. $M = 3.18 \times 10^5 \frac{\delta P}{1+z} M_{\odot}$ (thin accretion disk with a Schwarzschild black hole),
2. $M = 4.77 \times 10^5 \frac{\delta P}{1+z} M_{\odot}$ (thick accretion disk with a Schwarzschild black hole),
3. $M = 1.93 \times 10^6 \frac{\delta P}{1+z} M_{\odot}$ (Kerr black hole), where M_{\odot} is the solar mass.

Here $z = 0.306$ (K. Nilsson et al. 2010) and $\delta = 23.9$ (O. Hervet et al. 2016). If we choose $\Delta T_{\text{grlc}}^{\bar{T}}$ instead of the orbital period, the mass of central black hole should be from 2.50×10^8 to $1.52 \times 10^9 M_{\odot}$, with M_{\odot} being the solar mass.

4.3. The Irregular Intraday Variabilities

OJ 287 is a BL Lac object; its jet and accretion disk are therefore dominating the optical emission and give rise to the irregular IDV. To identify the emission mechanism we examine, day by day, the relation between flux density and spectral index (Figure 11); blue arrows trace the time evolution.

By incorporating the radiation framework of J. C. Isler et al. (2017), we can account for the distributions displayed in Figure 11.

1. On 2022 December 23, three emission stages are identified: (1) rising synchrotron emission, (2) radiative cooling, and (3) declining synchrotron flux.
2. On four days (2022 December 24, 2022 December 25, 2022 December 27, and 2023 January 28), the evolution follows three stages: (1) rising synchrotron emission, (2) radiative cooling, and (3) declining synchrotron emission.
3. On 2022 December 29, the first stage corresponds to declining synchrotron emission and the second stage corresponds to increasing synchrotron emission.
4. On 2023 January 4, the first stage is dominated by increasing synchrotron emission, the second by radiative cooling, and the third by declining synchrotron emission.

4.4. Conclusion

In this work, we used the 1.26 m NGT to monitoring the blazar OJ 287 during a period of 15 nights from 2022 December 4 to 2023 January 28. Based on the observations, we conclude the following points.

1. We found intraday optical variabilities at *gri*. About half of the observational nights display the IDV phenomenon, with the biggest variabilities being $\Delta m_g = 0.459 \pm 0.066$ mag at the *g* band, $\Delta m_r = 0.190 \pm 0.027$ mag at the *r* band, and $\Delta m_i = 0.399 \pm 0.064$ mag at the *i* band.
2. When we analyze the distribution differences from different bands, we find that the variable value Δm and VR show frequency-dependent properties, but the variable timescale (ΔT) and time differences between the adjacent peaks ($\Delta T'$) show frequency-independent properties.
3. In order to explain our results, we propose a model where the IDV phenomena are a combination of irregular and regular components, and where these different components have different physical origins.

Acknowledgments

We acknowledge the Guangdong Major Project of Basic and Applied Basic Research (grant No. 2024A1515013169) and science research grants from the China Manned Space Project with No. CMS-CSST-2021-A06. The work is partially supported by the National Natural Science Foundation of China (U2031112, NSFC U2031201). We acknowledge the

support of the staff of the Xinglong 1.26 m telescope. This work was partially supported by National Astronomical Observatories, Chinese Academy of Sciences.

ORCID iDs

Yu-Hai Yuan  <https://orcid.org/0000-0001-8395-1706>

References

- Abdo, A. A., Ackermann, M., Agudo, I., et al. 2010, *ApJ*, **716**, 30
 Acharyya, A., Adams, C. B., Archer, A., et al. 2024, *ApJ*, **973**, 134
 Bhatta, G., Zola, S., Stawarz, L., et al. 2016, *ApJ*, **832**, 47
 Bonning, E., Urry, C. M., Bailyn, C., et al. 2012, *ApJ*, **756**, 13
 Britzen, S., Fendt, C., Witzel, G., et al. 2018, *MNRAS*, **478**, 3199
 Brown, L. M. J., Robson, E. I., & Gear, W. K. 1989, *ApJ*, **340**, 150
 De Diego, J. A. 2010, *AJ*, **139**, 1269
 De Diego, J. A., Polednikova, J., Bongiovanni, A., et al. 2015, *AJ*, **150**, 44
 Dey, L., Valtonen, M. J., Gopakumar, A., et al. 2018, *ApJ*, **866**, 11
 Fan, J. H. 2005, *ChJAS*, **5**, 213
 Fan, J. H., Kurtanidze, O., Liu, Y., et al. 2017, *ApJ*, **837**, 45
 Fan, J. H., Kurtanidze, O., Liu, Y., et al. 2014, *ApJS*, **213**, 26
 Fan, J. H., Yang, J. H., Liu, Y., et al. 2016, *ApJS*, **226**, 20
 Fan, J. H., Yuan, Y. H., Wu, H., et al. 2019, *RAA*, **19**, 142
 Fiorucci, M., & Tosti, G. 1996, *A&AS*, **16**, 403
 Goyal, A., Stawarz, L., Zola, S., et al. *ApJ*, **863**, 175
 Gu, M. F., Lee, C. U., Pak, S., Yim, H. S., & Fletcher, A. B. 2006, *A&A*, **450**, 39
 Guo, Q., Xiong, D. R., Bai, J. M., et al. 2017, *RAA*, **17**, 8
 Gupta, A. C., Gaur, H., Wiita, P. J., et al. 2019, *AJ*, **157**, 95
 Gupta, A. C., Kushwaha, P., Valtonen, M. J., et al. 2024, *ApJ*, **960**, 11
 Heidt, J., & Wagner, S. J. 1996, *A&A*, **305**, 42
 Hervert, O., Boisson, C., & Sol, H. 2016, *A&A*, **592**, A22
 Huang, W. R., Xie, Z., Zhong, W. J., et al. 2020, *PASP*, **132**, 075001
 Hudec, R., Basta, M., Pihajoki, P., & Valtonen, M. 2013, *A&A*, **559**, A20
 Isler, J. C., Urry, C. M., Coppi, P., et al. 2017, *ApJ*, **844**, 107
 Kalita, N., Yuan, Y. H., Gu, M. F., et al. 2023, *ApJ*, **943**, 135
 Kinzel, W. M., Dickman, R. L., & Predmore, C. R. 1988, *Natur*, **331**, 48
 Massaro, E., Nesci, R., & Maesano, M. 1998, *MNRAS*, **299**, 47
 Nilsson, K., Takalo, L. O., Lehto, H. J., & Sillanpää, A. 2010, *A&A*, **516**, A60
 Sillanpää, A. 1991, *Ap&SS*, **176**, 297
 Sillanpää, A., Haarala, S., Valtonen, M. J., Sundelius, B., & Byrd, G. G. 1988, *ApJ*, **325**, 628
 Stickel, M., Fried, J. W., Kuehr, H., Padovani, P., & Urry, C. M. 1991, *ApJ*, **374**, 431
 Ulrich, M. H., Maraschi, L., & Urry, C. M. 1997, *ARA&A*, **35**, 445
 Urry, C. M., & Padovani, P. 1995, *PASP*, **107**, 803
 Valtaoja, E., Lehto, H., Teerikorpi, P., et al. 1985, *Natur*, **314**, 148
 Valtonen, M. J., Mikkola, S., Lehto, H. J., et al. 2011, *ApJ*, **742**, 22, 12
 Weaver, Z. R., Williamson, K. E., Jorstad, S. G., et al. 2020, *ApJ*, **900**, 137
 Wehrle Ann, E., Michael, C., & Witt Paul, J. 2019, *ApJ*, **877**, 151
 Wu, J. H., Zhou, X., Wu, X. B., et al. 2006, *AJ*, **132**, 1256
 Xiong, D., Bai, J., Zhang, H., et al. 2017, *ApJS*, **229**, 21
 Yuan, Y. H., Du, G. J., Fan, J. H., et al. 2023, *ApJS*, **269**, 60
 Yuan, Y. H., Fan, J. H., Wu, H., et al. 2021, *RAA*, **21**, 6
 Zheng, Y. G., Zhang, X., & Bi, X. W. 2007, *PASP*, **119**, 477
 Zhou, D. T., Zhang, Z. L., Gupta, A. C., et al. 2024, *MNRAS*, **532**, 3285